

X-RAY AND ROTATIONAL LUMINOSITY CORRELATION AND MAGNETIC HEATING OF THE RADIO PULSARS

S. SHIBATA¹ E. WATANABE² Y. YATSU³ T. ENOTO^{4, 5} AND A. BAMBA^{6, 7, 8}

¹ Department of Physics, Yamagata University, 1-4-12 Kojirakawa, Yamagata, JAPAN

² School of Science and Technology, Yamagata University, 1-4-12 Kojirakawa, Yamagata, JAPAN

³ Department of Physics, Tokyo Institute of Technology, 2-12-1 Ohokayama, Meguro, Tokyo 152-8551, Japan

⁴ The Hakubi Center for Advanced Research, Kyoto University, Kyoto 606-8302, Japan

⁵ Department of Astronomy, Kyoto University, Kitashirakawa-Oiwake-cho, Sakyo-ku, Kyoto 606-8502, Japan

⁶ Department of Physics and Mathematics, Aoyama Gakuin University, 5-10-1 Fuchinobe, Chuo-ku, Sagami-hara, Kanagawa 252-5258, Japan

⁷ Department of Physics, The University of Tokyo, 7-3-1 Hongo, Bunkyo-ku, Tokyo 113-0033, Japan

⁸ Research Center for the Early Universe, School of Science, The University of Tokyo, 7-3-1 Hongo, Bunkyo-ku, Tokyo 113-0033, Japan

ABSTRACT

Previous works have suggested a correlation between the X-ray luminosity L_x and the rotational luminosity L_{rot} of the radio pulsars. However, none of the obtained regression lines are statistically acceptable due to large scatters.

We construct a statistical model which has an intrinsic L_x - L_{rot} relation and reproduces the observed L_x distribution about it by using a Monte Carlo simulator, which takes into account the effects obscuring the intrinsic relation, i.e., the anisotropy of radiation, additional heating, uncertainty in distance and detection limit of the instruments.

From the ATNF pulsar catalog we collect 57 ‘ordinary radio pulsars’ with significant detection and 42 with upper limits. The sample does not include the high-magnetic field pulsars ($> 10^{13}$ G), which are separately analyzed.

We obtain a statistically acceptable relation $L_x(0.5-10\text{keV}) = 10^{31.69}(L_{\text{rot}}/L_0)^{c_1}$ with $c_1 = 1.03 \pm 0.27$ and $L_0 = 10^{35.38}$. The distribution about the obtained L_x - L_{rot} relation is reproduced well by the simulator.

Pulsars with abnormally high L_x fall into two types: one is the soft gamma-ray pulsars, and the other is thermally bright pulsars in comparison with the standard cooling curve. On the other hand, pulsars showing low L_x are found to have dim pulsar wind nebulae. We argue that there is an unknown mechanism that governs both the magnetospheric emission and the pulsar wind nebulae, and it might involve the production rate of electron-positron pairs.

The high-field pulsars form a distinctive population other than the ordinary pulsars due to their excess luminosities.

Keywords: pulsars; general – stars: neutron – X-rays: general

1. INTRODUCTION

Empirical relation between the high-energy luminosity and the rotational luminosity provides a good constraint on the emission and particle acceleration mechanisms of the pulsar magnetosphere. The rotational luminosity is given by $L_{\text{rot}} = 4\pi I \dot{P}/P^3$ where P is the observed pulse period, \dot{P} is its time derivative and I is the moment of inertia of the neutron star, which is assumed to be $\approx 10^{45} \text{g cm}^2$. (The standard deviation of the neutron star mass is ~ 0.2 solar masses, which is ~ 0.1 in log-scale (Ozel et al. 2015, Kiziltan et al. 2013), so the constancy of I would not affect the present statistical

study. The proper motion, $\sim 450 \text{ km s}^{-1}$, is also unimportant in determining L_{rot} .) *Fermi* LAT observations have indicated that the gamma-ray luminosities L_γ follow $L_\gamma \propto L_{\text{rot}}^{1/2}$ for young pulsars (Abdo et al. 2013), while the X-ray luminosities show a steeper correlation (Becker & Truemper 1997), which may be roughly represented by $L_x \sim 10^{-3} L_{\text{rot}}$. The slope of one half implies that the gamma-rays originate from the primary particles the flux of which is proportional to the Goldreich-Julian current $\sim (L_{\text{rot}}/c)^{1/2}$. On the other hand, a steeper slope in L_x - L_{rot} relation may be due to the fact that secondary pairs are attributed to X-ray radiation. A further implication on the L_γ - L_{rot} relation is the

change of the slope from one half to about unity when L_{rot} is decreased (Marelli et al. 2011). This indicates that some qualitative change in the particle acceleration and/or emission mechanisms when the available voltage is reduced to $\sim 10^{13}$ Volt. Takata et al. (2011) show that the outer gap model accounts for this change.

Even though the recent observations from the X-ray satellites such as *Chandra* and *XMM-Newton* provides high-quality spectral data for significant numbers of objects, the $L_x - L_{\text{rot}}$ correlation is still quite uncertain. The first identification of the correlation $L_x = 10^{-16.8} L_{\text{rot}}^{1.39}$ was suggested by Seward and Wang (1988). Later several suggestions have been made; $L_x = 10^{-3} L_{\text{rot}}$ (Becker and Truemper, 1997), $L_x = 10^{-12} L_{\text{rot}}^{1.5}$ (Saito 1998), $L_x = 10^{-15.34} L_{\text{rot}}^{1.34}$ (Possenti et al. 2002), $L_x = 10^{-0.8} L_{\text{rot}}^{0.92}$ (Li et al. 2008), $L_x = 10^{-3.24} L_{\text{rot}}^{0.997}$ in the 0.1–2 keV, and $L_x = 10^{-15.72} L_{\text{rot}}^{1.336}$ in the 2–10 keV (Becker 2009). The difference in the slopes may be due to the choice of energy bands and of the components: thermal, non thermal and pulsar wind nebula (PWN). All these works suggest correlations with linear regressions. Nevertheless, none of the regression lines are statistically acceptable, i.e., scatter about the regression lines are significant (Possenti et al. 2002, Kargaltsev et al. 2012).

Figure 1 shows the $L_x - L_{\text{rot}}$ plot for our sample, which is described in detail in §2. The open squares indicate the ordinary radio pulsars. It indicates a correlation between L_x and L_{rot} . However, a large scatter can also be seen. As suggested by Kargaltsev et al. (2012), the scatter is too large to be explained by incorrectly determined distances. Some pulsars appear to be much dimmer than the regression lines suggested earlier the solid line in Figure 1). This may be a geometrical effect, with which the phase averaged flux tends to be smaller than the true flux depending on viewing angles: the observed flux can be very small if the viewing angle is bad. Some authors suggest a critical line below which all the data locate, i.e., $L_x < 10^{-18.5} L_{\text{rot}}^{1.48}$ (Possenti et al. 2002), and $L_x < 10^{-21.4} L_{\text{rot}}^{1.51}$ (Kargaltsev et al., 2012). Because large scatter is also seen in the luminosity of PWN, these authors have suggested that some unknown physics (or other effect) restrains the X-ray luminosity. We will discuss this point in section 5. Observational detection limits could also affect the $L_x - L_{\text{rot}}$ plot; a dim object may not be observed if its distance is large. This selection effect brings about less distribution below an expected correlation when L_{rot} is small.

We take into account the above-mentioned effects in a Monte Carlo simulator and compare the simulated distribution with the observed data, and thereby we attempt to find a statistically acceptable ‘hidden’ relation between L_x and L_{rot} . We also statistically-test the distribution about the $L_x - L_{\text{rot}}$ relation. This test enables

us to search for characteristic of the scatter.

Another reason the $L_x - L_{\text{rot}}$ correlation may be contaminated is the X-ray radiation which is not caused by the rotational energy and therefore not related to L_{rot} . There are noticeable neutron star populations other than the rotation powered pulsars; more specifically they are the magnetars which is a joint population of anomalous X-ray pulsar (AXP) and soft gamma-ray repeater (SGR), the central compact object (CCO), the X-ray isolated neutron star (XINS). All these objects show excess X-ray luminosity. The origin is supposed to be the neutron star cooling radiation and dissipation of magnetic field.

Let us briefly summarize the properties of these X-ray sources. Persistent luminosity of magnetars taken from the McGill Magnetar Catalogue (Olausen & Kaspi, 2014) are included in Figure 1. The main characteristics of a proto-typical magnetars are (1) persistent X-ray luminosity in the range $10^{33} - 10^{36} \text{erg s}^{-1}$, which exceeds L_{rot} , (2) high time-variability and (3) large braking torque, which implies the surface dipole field of $B_d \sim 10^{14} - 10^{15}$ G (see e.g., Turolla et al. 2015 for a review), where the dipole field is derived from P and \dot{P} by

$$B_d = \left(\frac{3}{2} \frac{Ic^3}{(2\pi)^2 R_*^6} P \dot{P} \right)^{1/2} \quad (1)$$

$$\approx 1.1 \times 10^{12} \text{G} \left(\frac{P}{1\text{s}} \frac{\dot{P}}{10^{-15}} \right)^{1/2}, \quad (2)$$

where $R_* \approx 10^6$ cm is the radius of the neutron star. By definition, the high X-ray luminosity and bursting activity of the magnetars are powered by their strong magnetic fields (Duncan & Thompson, 1992). However, it was found recently that SGR 0418+5729 has a dipole field of $B_d \sim 6.1 \times 10^{12}$ G (Esposito et al., 2010; Rea et al., 2010; Rea et al., 2013), which is well inside the range of ordinary radio pulsars. This fact suggests that the magnetic field of magnetars is in multipole components B_m , which can be larger than and independent of B_d . The origin of B_m may be a large toroidal field in the crust. In the theoretical point of view, Ciolfi & Rezzolla (2013) shows that the toroidal field can be much stronger than the poloidal field.

CCOs are bright X-ray sources which reside near the centers of SNRs. The spin down parameters of three CCOs (PSR J1852+0040 in Kes 79, PSR 0821–4300 in Puppis A and 1E1207.4–5209 in PKS 1209–51/52) are measured (Halpern & Gotthelf 2010, Gotthelf et al. 2013). It is suggested that ages of CCOs are much larger than those of SNRs, and they have small magnetic field, $B_d \sim 10^{10}$ G (e.g., Bogdanov et al. 2014). The X-ray luminosity of these three CCOs are also plotted in Figure 1. Their positions in the $L_x - L_{\text{rot}}$ plot

are obviously apart from the general trend of the radio pulsars and rather in the end of the magnetar group. Although B_d is small, presently-‘hidden’ or past strong crust field may exist. All the known CCOs exhibit no radio emission. However, their locations in $P - \dot{P}$ diagram are within the range of the ordinary radio pulsars. This suggests that the ordinary radio pulsars associated with SNR may have dissipative crustal field similar to CCOs. This possibility was examined for nearby objects (< 6 kpc) by Bogdanov et al. (2014), who found no X-ray excess emission in their sample.

Several tens of radio pulsars are known to have dipole fields larger than $\sim 10^{13}$ G. PSR J1718-3718 and PSR J1734-3333, respectively, have $B_d = 7.47 \times 10^{13}$ G and $B_d = 5.23 \times 10^{13}$ G, which are comparable with 5.9×10^{13} G of the AXP 1E 2259+586. At present, three of the high-magnetic field pulsars exhibit large X-ray luminosity ($> 0.1 L_{\text{rot}}$). If B_m is independent of B_d , ordinary radio pulsars may have dissipative crustal field, such as those seen in magnetars and X-ray excess luminosity. Occurrence rate of such excess may depend on B_d or on the evolutionary path in $P - \dot{P}$ diagram. Another important fact on the high-magnetic field pulsar is that PSR J1846-0258 with $B_d = 5 \times 10^{13}$ G was thought to be a rotation powered pulsar (though radio quiet) but showed X-ray outbursts in a way commonly seen in the magnetars (Gavriil et al. 2008). Quite recently, the radio pulsar J1119-6127 with $B_d \sim 4.1 \times 10^{13}$ G exhibited a magnetar-like outburst, adding the second example (Younes et al. 2016; Kennea et al. 2016; Archibald et al. 2016). This suggests that some of ordinary radio pulsars may have dissipative magnetic fields, which are not always in the dipole field but may be in crustal multipole fields. If dissipation is sudden, it causes outbursts, while gradual dissipation would cause an excess of the persistent X-ray luminosity or a high surface temperature as compared with standard cooling curves of the neutron star. If this is the case, magnetic heating could cause scatter in the $L_x - L_{\text{rot}}$ plot of the ordinary radio pulsars.

In this paper, we investigate statistical properties of the $L_x - L_{\text{rot}}$ plot, searching for an intrinsic $L_x - L_{\text{rot}}$ relation. We discuss the difference between the ordinary radio pulsars and the high-magnetic field pulsars. We also discuss the origin of the scatter: why some pulsars show considerably large L_x while some show very small L_x .

The paper is organized as follows: observational data are accumulated and the statistical samples are provided in § 2, the method of statistical analysis is given in § 3, and the result is given in § 4 and discussed in § 5.

2. SAMPLE PREPARATION

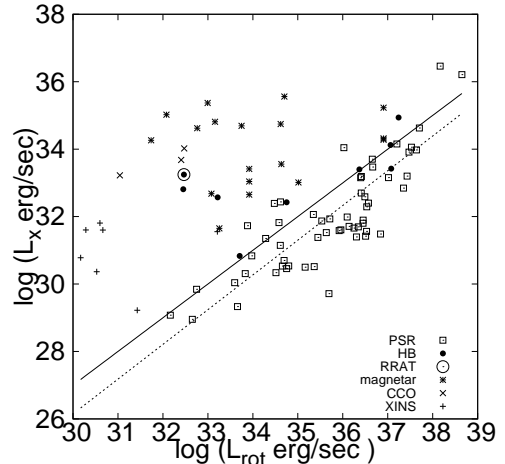


Figure 1. The $L_x - L_{\text{rot}}$ plot for our sample and related objects. The open squares and the filled circles are, respectively, for Sample SAB (ordinary radio pulsars) and Sample HB (high-magnetic field pulsars) defined in section 2. The data for other neutron stars, the magnetars (Olausen & Kaspi 2014), CCO (Halpern & Gotthelf 2010), and XINS (Viganò et al. 2013) are superposed. The large open circle indicates RRAT. The dashed line is the best fit model relation obtained in section 4 while the solid line is the earlier suggestion $L_x = 10^{-3} L_{\text{rot}}$ (Becker & Truemper, 1997).

To define our sample, we use the ATNF pulsar catalogue¹ (Manchester et al. 2005), and make a set of ‘ordinary’ radio pulsars satisfying following conditions: (1) its P , \dot{P} and the distance d are available, (2) it is observed in radio, (3) not a magnetar; neither AXP nor SGR², (4) not a millisecond pulsar (MSP) (filtered by $B_d > 10^{10}$ G), (to exclude a possible effect of history of accretion), (5) not in a binary system. Since the catalog provides the best estimate distance rather than the dispersion measure distance if it is available, we use the best estimate distance in the catalog. There are two main reasons we exclude MSPs in the present sample. The weak field of MSP is thought to be due to mass accretion, so that ‘buried’ field might exist and causes additional heating (Bejger et al., 2011). From the observational point of view, the study of the second Fermi catalog (Abdo et al., 2013) suggests that gamma-X ratios of the ordinary pulsar and MSP are different.

After the filtering, we list a high-magnetic field sample out of the obtained set with the condition $B_d > 10^{13}$ G to define ‘Sample HB’. The remaining pulsars are the ‘ordinary’ radio pulsars and are separated into five groups according to the ‘rotational en-

¹ Available at <http://www.atnf.csiro.au/research/pulsar/psrcat/>.

² The objects listed in McGill magnetar catalog (Olausen & Kaspi 2014; <http://www.physics.mcgill.ca/pulsar/magnetar/main.html>) or indicated by AXP in the ATNF catalogue are removed.

ergy flux’ defined by $F_{\text{rot}} = L_{\text{rot}}/4\pi d^2$, i.e., ‘Sample S’ ($F_{\text{rot}} > 10^{-9}$ erg/cm²s⁻¹), ‘Sample A’ ($10^{-9} \geq F_{\text{rot}} > 10^{-10}$ erg/cm²s⁻¹), ‘Sample B’ ($10^{-10} \geq F_{\text{rot}} > 10^{-11}$ erg/cm²s⁻¹), ‘Sample C’ ($10^{-11} \geq F_{\text{rot}} > 10^{-12}$ erg/cm²s⁻¹) and ‘Sample D’ ($10^{-12} \geq F_{\text{rot}}$ erg/cm²s⁻¹). Since the lowest value of F_{rot} for Sample B is 10^{-11} erg/cm²s⁻¹, its expected flux would be $\approx 10^{-14}$ erg/cm²s⁻¹, which is roughly the detection limit of the current instruments with typical exposure times. This means that still dimmer Samples C and D are not useful in determining the $L_x - L_{\text{rot}}$ relation. In our statistical analysis, we use the joint Sample S+A+B (simply denoted by ‘Sample SAB’) and Sample HB. To see selection effect, we also use Sample S, A and B separately.

We review the data of the listed pulsars in the literature. Using the reported models for the observed unabsorbed flux, we convert them into the values in the 0.5–10 keV band. As has been mentioned in the previous section, we are interested in the possibility of magnetic heating in the ordinary radio pulsars, so that the choice is the 0.5–10 keV band rather than 2–10 keV. As for the most of the detected data, we use the flux corrected for the presence of a nebula component, if available. We

use the distances cited in the ATNF pulsar catalogue to obtain the luminosity (not the values in the original papers). Since uncertainty in the distance causes scattering in L_x , this effect is taken into account the probability density distribution obtained by the Monte Carlo simulator. In our statistical analysis, we also use the upper limit when they are available. Apart from reviewing the past publications, we searched HEASARC archive data for all the pulsars in Sample S, A, B and HB. Only for PSR J1909+0749, there is no published data, but we find a HEASARC archive data for serendipitous pointing toward the object and find an upper limit of $L_x < 9.648 \times 10^{-14}$ erg/cm²s⁻¹ in the 0.5 – 10 keV band assuming the power law model with a photon index of 1.5 (detail is given in Appendix B). There are 61 objects in Sample SAB and 41 objects in Sample HB, for which no observation is made or the obtained upper limit is too large and useless ($> 10^{-2}L_{\text{rot}}$). The sample names have subscripts ‘d’ or ‘ul’ to indicate if detected values or upper limits, i.e., Sample S_d, Sample S_{ul}, Sample A_d, Sample A_{ul} and so on. The numbers of samples for each subset are summarized in Table 1. The data sets are given in Table 2 and shown in Figure 2.

Table 2. $L_x - L_{\text{rot}}$ data for all the samples

Name PSR	Period s	distance kpc	$\log L_{\text{rot}}$ erg s ⁻¹	$\log L_x$ erg s ⁻¹	$\log(L_x/L_{\text{rot}})$	References
Sample S _d						
B0531+21	0.033	2.00	38.650	36.209	-2.44	Kargaltsev & Pavlov 2008
B0656+14	0.385	0.28	34.581	31.821	-2.76	De Luca et al., 2005
B0833-45	0.089	0.28	36.840	31.483	-5.36	Kargaltsev & Pavlov 2008
B0906-49	0.107	1.00	35.693	29.715	-5.98	Kargaltsev et al. 2012
B1046-58	0.124	2.90	36.303	31.396	-4.91	Kargaltsev & Pavlov 2008
B1706-44	0.102	2.60	36.533	32.289	-4.24	Kargaltsev & Pavlov 2008
B1757-24	0.125	4.61	36.413	33.188	-3.23	Kargaltsev & Pavlov 2008
B1823-13	0.101	4.12	36.454	31.895	-4.56	Kargaltsev & Pavlov 2008
B1951+32	0.040	3.00	36.572	32.400	-4.17	Kargaltsev & Pavlov 2008
B2334+61	0.495	0.70	34.797	30.537	-4.26	McGowan et al., 2006
J0205+6449	0.066	3.20	37.431	33.201	-4.23	Kargaltsev & Pavlov 2008
J0633+1746	0.237	0.25	34.513	30.337	-4.18	Kargaltsev & Pavlov 2008
J1357-6429	0.166	4.09	36.491	32.588	-3.90	Kargaltsev & Pavlov 2008
J1400-6325	0.031	7.00	37.705	34.628	-3.08	Renaud et al., 2010
J1420-6048	0.068	7.65	37.015	33.157	-3.86	Kargaltsev & Pavlov 2008
J1524-5625	0.078	3.84	36.508	31.418	-5.09	Kargaltsev et al. 2012
J1617-5055	0.069	6.46	37.203	34.152	-3.05	Kargaltsev & Pavlov 2008
J1732-3131	0.197	0.80	35.163	30.500	-4.66	Ray et al., 2011,
J1740+1000	0.154	1.36	35.365	30.515	-4.85	Kargaltsev & Pavlov 2008
J1747-2809	0.052	17.55	37.638	33.977	-3.66	Porquet et al., 2003
J1747-2958	0.099	2.49	36.399	33.152	-3.25	Kargaltsev & Pavlov 2008

Table 1. Summary of the Numbers of our Samples.

Sample Name	Range	total	detected	upper limit	not observed
S	$F_{\text{rot}} > 10^{-9}$	29	27	2	0
A	$10^{-9} \geq F_{\text{rot}} > 10^{-10}$	43	20	15	8
B	$10^{-10} \geq F_{\text{rot}} > 10^{-11}$	88	10	25	53
SAB	$F_{\text{rot}} > 10^{-11}$	160	57	42	61
HB	$B_d > 10^{13}$	56	9	6	41

Table 2. (continued)

Name	Period	distance	$\log L_{\text{rot}}$	$\log L_x$	$\log(L_x/L_{\text{rot}})$	References
PSR	s	kpc	erg s^{-1}	erg s^{-1}		
J1809-1917	0.083	3.71	36.249	31.659	-4.59	Kargaltsev & Pavlov 2008
J1833-1034	0.062	4.10	37.527	34.057	-3.47	Kargaltsev & Pavlov 2008
J1907+0602	0.107	3.01	36.451	31.804	-4.65	Abdo et al., 2010
J2021+3651	0.104	1.80	36.529	31.562	-4.97	Kargaltsev & Pavlov 2008
J2022+3842	0.049	10.00	37.472	33.913	-3.56	Marthi et al., 2011
J2229+6114	0.052	3.00	37.351	32.845	-4.51	Kargaltsev & Pavlov 2008
Sample S_{ul}						
B1742-30	0.367	0.20	33.930	< 28.683	< -5.25	Prinz & Becker 2015
J1913+1011	0.036	4.48	36.458	< 31.029	< -5.43	Prinz & Becker 2015
Sample A_d						
B0114+58	0.101	2.14	35.345	32.063	-3.28	Prinz & Becker 2015
B0355+54	0.156	1.00	34.657	30.533	-4.12	Kargaltsev & Pavlov 2008
B0540-69	0.050	53.70	38.167	36.462	-1.70	Kaaret et al., 2001
B1055-52	0.197	1.53	34.478	32.392	-2.09	De Luca et al., 2005
B1338-62	0.193	8.55	36.141	31.710	-4.43	Prinz & Becker 2015
B1800-21	0.134	4.40	36.345	31.695	-4.65	Kargaltsev & Pavlov 2008
B1822-09	0.769	0.30	33.659	29.331	-4.33	Prinz & Becker 2015
B1853+01	0.267	3.30	35.633	31.525	-4.11	Kargaltsev & Pavlov 2008
B1929+10	0.227	0.31	33.595	30.041	-3.55	Kargaltsev & Pavlov 2008
J0538+2817	0.143	1.30	34.694	30.698	-4.00	Kargaltsev & Pavlov 2008
J0729-1448	0.252	4.37	35.447	31.381	-4.07	Kargaltsev et al. 2012
J1016-5857	0.107	9.31	36.411	32.699	-3.71	Kargaltsev & Pavlov 2008
J1028-5819	0.091	2.76	35.920	31.585	-4.34	Kargaltsev et al. 2012
J1509-5850	0.089	3.85	35.712	31.930	-3.78	Kargaltsev & Pavlov 2008
J1531-5610	0.084	3.10	35.957	31.605	-4.35	Kargaltsev et al. 2012
J1702-4128	0.182	5.18	35.534	31.870	-3.66	Kargaltsev et al. 2012
J1718-3825	0.075	4.24	36.097	31.988	-4.11	Kargaltsev et al. 2012
J1741-2054	0.414	0.30	33.977	30.837	-3.14	Camilo et al., 2009
J1856+0245	0.081	10.29	36.665	33.469	-3.20	Rousseau et al., 2012
J2043+2740	0.096	1.13	34.752	30.456	-4.29	Abdo et al., 2013
Sample A_{ul}						
B0740-28	0.167	2.00	35.155	< 30.979	< -4.18	Prinz & Becker 2015
B1727-33	0.139	4.26	36.091	< 31.146	< -4.95	Prinz & Becker 2015
B1830-08	0.085	4.50	35.766	< 33.045	< -2.72	Kargaltsev et al., 2012
J0248+6021	0.217	2.00	35.328	< 32.564	< -2.76	Abdo et al., 2013

Table 2. (continued)

Name	Period	distance	$\log L_{\text{rot}}$	$\log L_x$	$\log(L_x/L_{\text{rot}})$	References
PSR	s	kpc	erg s^{-1}	erg s^{-1}		
J0940-5428	0.088	4.27	36.287	< 30.870	< -5.42	Prinz & Becker 2015
J1105-6107	0.063	7.07	36.393	< 31.390	< -5.00	Prinz & Becker 2015
J1637-4642	0.154	5.77	35.806	< 31.845	< -3.96	Prinz & Becker 2015
J1702-4310	0.241	5.44	35.803	< 31.417	< -4.39	Prinz & Becker 2015
J1739-3023	0.114	3.41	35.478	< 31.291	< -4.19	Prinz & Becker 2015
J1828-1101	0.072	7.26	36.194	< 31.983	< -4.21	Prinz & Becker 2015
J1831-0952	0.067	4.33	36.033	< 32.191	< -3.84	Prinz & Becker 2015
J1835-1106	0.166	3.08	35.250	< 30.777	< -4.47	Prinz & Becker 2015
J1837-0604	0.096	6.19	36.301	< 32.193	< -4.11	Prinz & Becker 2015
J1841-0345	0.204	4.15	35.430	< 31.297	< -4.13	Prinz & Becker 2015
J1928+1746	0.069	8.12	36.206	< 31.599	< -4.61	Prinz & Becker 2015
Sample B _d						
B0540+23	0.246	3.54	34.611	31.148	-3.46	Prinz & Becker 2015
B0628-28	1.244	0.32	32.164	29.078	-3.09	Tepedelenlioglu & Ögelman 2005
B0823+26	0.531	0.32	32.655	28.952	-3.70	Becker et al., 2004
B0919+06	0.431	1.10	33.831	30.309	-3.52	Prinz & Becker 2015
B0950+08	0.253	0.26	32.748	29.845	-2.90	Becker et al., 2004
B1221-63	0.216	4.00	34.285	31.351	-2.93	Prinz & Becker 2015
B1822-14	0.279	5.45	34.615	32.436	-2.18	Bogdanov et al., 2014
J0855-4644	0.065	9.90	36.025	34.044	-1.98	Acero et al., 2013
J1112-6103	0.065	30.00	36.657	33.703	-2.95	Prinz & Becker 2015
J1301-6310	0.664	2.06	33.881	31.729	-2.15	Prinz & Becker 2015
Sample B _{dl}						
B0136+57	0.272	2.60	34.320	< 30.869	< -3.45	Prinz & Becker 2015
B1356-60	0.127	5.00	35.082	< 32.113	< -2.97	Prinz & Becker 2015
B1449-64	0.179	2.80	34.273	< 31.041	< -3.23	Prinz & Becker 2015
B1634-45	0.119	3.83	34.876	< 31.857	< -3.02	Prinz & Becker 2015
B1643-43	0.232	6.86	35.555	< 32.933	< -2.62	Prinz & Becker 2015
B1702-19	0.299	1.18	33.786	< 30.437	< -3.35	Prinz & Becker 2015
B1730-37	0.338	3.44	34.187	< 31.618	< -2.57	Prinz & Becker 2015
B1754-24	0.234	3.51	34.599	< 31.384	< -3.22	Prinz & Becker 2015
B1758-23	0.416	4.00	34.793	< 31.693	< -3.10	Prinz & Becker 2015
B1828-11	0.405	3.58	34.552	< 31.953	< -2.60	Prinz & Becker 2015
J0631+1036	0.288	6.54	35.240	< 31.887	< -3.35	Kennea et al., 2002,
J1055-6028	0.100	30.00	36.070	< 32.940	< -3.13	Prinz & Becker 2015
J1406-6121	0.213	9.11	35.349	< 32.557	< -2.79	Prinz & Becker 2015
J1412-6145	0.315	9.32	35.095	< 32.063	< -3.03	Prinz & Becker 2015
J1413-6141	0.286	11.00	35.751	< 32.230	< -3.52	Prinz & Becker 2015
J1514-5925	0.149	4.50	34.538	< 32.106	< -2.43	Prinz & Becker 2015
J1648-4611	0.165	5.71	35.319	< 31.262	< -4.06	Prinz & Becker 2015
J1723-3659	0.203	4.28	34.579	< 32.100	< -2.48	Prinz & Becker 2015
J1815-1738	0.198	9.01	35.595	< 33.029	< -2.57	Prinz & Becker 2015
J1828-1057	0.246	4.27	34.738	< 31.612	< -3.13	Prinz & Becker 2015
J1838-0549	0.235	4.73	35.005	< 31.727	< -3.28	Prinz & Becker 2015

Table 2. (continued)

Name	Period	distance	$\log L_{\text{rot}}$	$\log L_x$	$\log(L_x/L_{\text{rot}})$	References
PSR	s	kpc	erg s ⁻¹	erg s ⁻¹		
J1850-0026	0.167	10.69	35.523	< 32.159	< -3.36	Prinz & Becker 2015
J1907+0918	0.226	7.68	35.508	< 31.064	< -4.44	Prinz & Becker 2015
J1908+0734	0.212	0.58	33.532	< 30.307	< -3.22	Prinz & Becker 2015
J1909+0749	0.237	10.84	35.653	< 33.131	< -2.52	this work
Sample HB _d						
B1509-58	0.151	4.40	37.242	34.938	-2.30	Kargaltsev & Pavlov 2008
B1916+14	1.181	1.41	33.706	30.834	-2.87	Zhu et al., 2009
J0726-2612	3.442	3.01	32.453	32.812	* 0.36	Speagle et al., 2011
J1119-6127	0.408	8.40	36.369	33.400	-2.97	Safi-Harb & Kumar 2008
J1124-5916	0.135	5.00	37.077	33.422	-3.66	Kargaltsev & Pavlov 2008
J1718-3718	3.379	5.08	33.217	32.571	* -0.65	Zhu et al., 2011
J1734-3333	1.169	7.40	34.750	32.425	-2.33	Olausen et al., 2013
J1819-1458	4.263	3.81	32.467	33.244	* 0.78	McLaughlin et al., 2007
J1930+1852	0.137	7.00	37.063	34.123	-2.94	Kargaltsev & Pavlov 2008
Sample HB _{ul}						
B0154+61	2.352	1.61	32.758	< 30.285	< -2.47	Prinz & Becker 2015
B1610-50	0.232	7.24	36.196	< 33.242	< -2.95	Pivovaro et al., 1998
J1524-5706	1.116	21.59	34.005	< 31.961	< -2.04	Prinz & Becker 2015
J1726-3530	1.110	9.97	34.547	< 32.113	< -2.43	Prinz & Becker 2015
J1841-0524	0.446	4.89	35.018	< 31.639	< -3.38	Prinz & Becker 2015
J1846-0257	4.477	4.69	31.850	< 29.603	< -2.25	Prinz & Becker 2015

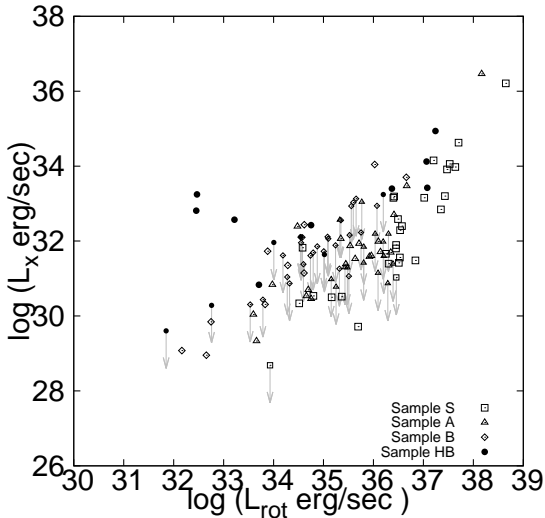


Figure 2. The $L_x - L_{\text{rot}}$ plot for our sample in Table 2. The upper limit values are indicated by the arrows.

3. METHOD OF ANALYSIS

The data set for each pulsar contains (L_x, L_{rot}, d) , where L_x and L_{rot} are measured in erg sec^{-1} , and d is in kpc. Let $y = \log L_x$, $a = \log L_{\text{rot}}$, and for the i -th pulsar in particular, denoting y_i and a_i . We assume that

there is an intrinsic model relation between L_x and L_{rot} , which is represented by a linear formula,

$$y_{\text{model}}(a) = c_1(a - 37) + c_2, \quad (3)$$

where c_1 and c_2 are the constants. The random variable we consider is the residuals defined by

$$x = y - y_{\text{model}}(a). \quad (4)$$

We use a Monte Carlo simulator which produces a large number of simulated L_x for a given pulsar and construct a probability density function $f(x)$. The simulator takes into account possible effects which cause scatter in the $L_x - L_{\text{rot}}$ plot. The detail of the simulation will be discussed in the next subsection. If the model relation y_{model} is correctly guessed and if the simulator reproduces the statistical characteristics of the observation data properly, then the observation x follows the probability distribution $f(x)$. This is the hypothesis test to be performed.

3.1. The Monte Carlo Simulator

The simulator works in the following way.

For a given pulsar with a , the expected X-ray luminosity is given by $L_x^{\text{model}} = 10^{y_{\text{model}}(a)}$ from (3). The simulator produces residuals x by using a random num-

ber generator as described below. Once x is obtained, a simulated value of the X-ray luminosity is given by $\log L_x = x + y_{\text{model}}$.

The first step of the simulation is to include the geometrical effect. If the radiation is isotropic from whole the star, one would simply observe the value L_x^{model} . However, if it is from a small hot area on the star, one would observe $L_x = L_x^{\text{model}} \cos \theta$, where θ is the angle of the observer to the normal of the emitting surface. For a randomly oriented object, the probability density of observing L_x is given by

$$f(L_x) = \begin{cases} \frac{1}{2L_x^{\text{model}}} & \text{if } 0 \leq L_x \leq L_x^{\text{model}} \\ 0 & \text{if } L_x^{\text{model}} < L_x. \end{cases} \quad (5)$$

This simply means that L_x distributes uniformly in between L_x^{model} and zero when a hot spot is observed by randomly distributed observers (for derivation, see Appendix A). Since the star rotates, the viewing angle θ oscillates through one rotation, and therefore the value of θ is regarded as the mean value.

The magnetospheric radiation would have a higher anisotropy along the local magnetic field of the particle acceleration region. A simple extension for geometrical effect would be obtained if we introduce an index n and assume $L_x = L_x^{\text{model}} \cos^n \theta$. In the simulator, we model the effect of anisotropy in such a way that $n = 0$ for the isotropic radiation, $n = 1$ for the radiation from a small hot area on the star, and $n > 1$ for the magnetospheric directed radiation. In this general case, after transforming from L_x to x , we have

$$f(x) = \begin{cases} (1/n) \exp(x/n) & \text{if } x \leq 0 \\ 0 & \text{if } x > 0. \end{cases} \quad (6)$$

According to this probability, the simulator produces a number x_I , which yields a X-ray luminosity affected by the geometrical effect as $\log L_x^{\text{psr}} = x_I + y_{\text{model}}$. Thus dim pulsars are distributed below y_{model} (see the left top panel of Figure 3).

In the second step, we include the effect that dissipation of the crustal magnetic field may add some amount of X-ray luminosity. However, we know little about the property of this kind of radiation. We introduce two parameters: (1) \mathcal{P}_{mag} is the probability that such an excess emission appears, and (2) \hat{L}_x^{mag} is the largest luminosity below which the additional excess luminosity, L_x^{mag} , is uniformly distributed. Again with the random number generator, we find whether the excess radiation exists or not, and if it exists, L_x^{mag} is given. By adding the two components, we have a residual in the second step as

$$x_{\text{II}} = \log(L_x^{\text{psr}} + L_x^{\text{mag}}) - y_{\text{model}}. \quad (7)$$

In the third step, we consider uncertainties in the

estimated distance and interstellar absorption. The probability density function for this fluctuation is usually assumed to follow a log-normal distribution. He et al.(2013) examined the correlations among n_H , the dispersion measure DM and the distances obtained by other methods. From their Table 1, we obtain a distribution of residuals from the linear regression $\log n_H = 0.3508 + \log DM$ and make the Kolmogorov-Smirnov (KS) test for it. We find that the distribution fits very well with the log-normal distribution with the KS test statistics $D = 7.06 \times 10^{-2}$ and the significance level of $\mathcal{P}_{\text{KS}} = 91.64\%$, where we use `ksone` given in ‘‘Numerical Recipes’’ (Press et al. 1992). From the same table, we obtain the standard deviation for the difference between the dispersion measure distance and the distances measured by parallax or HI absorption to be $\sigma_{\text{dist}} = 0.35$.

The scatter in L_x could also be caused by errors in determining n_H and consequently the unabsorbed flux. This effect strongly depends on the statistical quality of the spectral fitting for each pulsar. The standard deviation of the errors in the unabsorbed flux in Kargaltsev & Pavlov(2008) is found to be 0.14 in log-scale. This indicates that the scatter due to uncertainty in the absorption is not as large as that of the distance squared, whose standard deviation is $2\sigma_{\text{dist}} = 0.7$.

Regarding these points, we assume a scatter δ according to a log-normal distribution with standard deviation of σ in the simulator. The value of σ is the model parameter, but it is constrained to be $\sigma \sim 0.7$. We add δ for the third step:

$$x_{\text{III}} = x_{\text{II}} + \delta, \quad (8)$$

by which a X-ray luminosity $\log L_x = x_{\text{III}} + y_{\text{model}}$ is obtained.

Finally, we take the observable flux limit into account. In the simulator, we use a parameter F_{lim} which defines the detection limit. If the value of L_x obtained in the third step is larger than $4\pi d^2 F_{\text{lim}}$, the final value x_{III} is taken as an observation x , otherwise it is thrown out.

The above process is repeated N times, where N is typically 2×10^4 for each pulsar to have stable results. Thus the simulated values of x yield the probability density function $f(x)$.

In summary, the model parameters are c_1 and c_2 for the model relation, n for anisotropy, \mathcal{P}_{mag} and \hat{L}_x^{mag} for excess radiation by magnetic field decay, σ for scattering due to the distance estimate and the interstellar absorption, and F_{lim} for the detection limit of the instruments. Typical distributions after each of the four steps is shown in Figure 3.

3.2. Method of Statistical Test

In this subsection, we describe the statistical test we have used to see if a given sample follows a specific

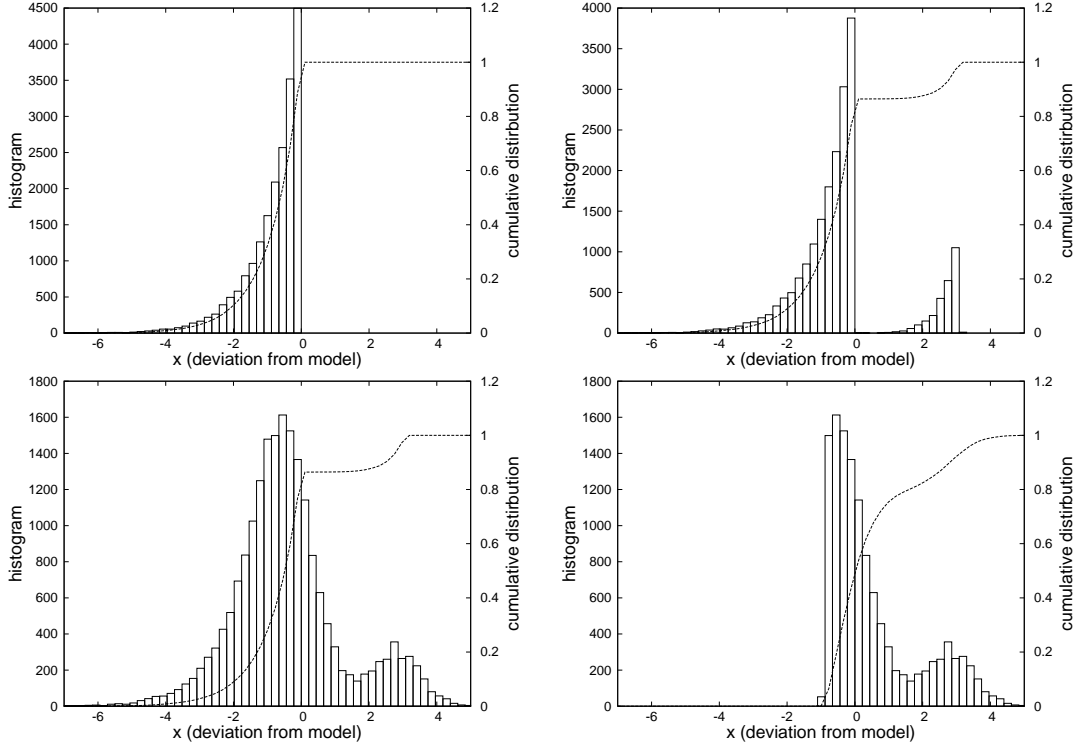


Figure 3. The distributions of a simulated L_x (histogram) and their cumulative distribution $g_i(x)$ (dotted curve) in each simulation step. The first step (upper left): including the effect of anisotropy, the second step (upper right): adding the excess emission, the third step (lower left): scattered by uncertain distance estimate and interstellar absorption, and the last step (lower right): the final distribution after the cut-off by the detection limit. Note that the distributions are different object by object, depending on L_{rot} and d , even if the simulation parameters are the same.

model. For a given sample, we have the observations $\{x_i, a_i, d_i\}$ where $i = 1, 2, \dots, N_{\text{psr}}$, and N_{psr} is the number of the pulsars. For each pulsar, the Monte Carlo simulator provides the probability density function $f_i(x)$. It is notable that $f_i(x)$ is given for each pulsar, which has the rotation power a_i and the distance d_i as known. The simulator takes the values of a_i and d_i into account and applies the assumed set of the model parameters $\{c_1, c_2, n, \mathcal{P}_{\text{mag}}, \hat{L}_x^{\text{mag}}, F_{\text{lim}}\}$. To be exact, $f_i(x)$ may be written as $f_i(x, a_i, d_i; n, \mathcal{P}_{\text{mag}}, \hat{L}_x^{\text{mag}}, F_{\text{lim}})$.

The random variable x_i is now transformed into a new variable ξ_i by using the cumulative distribution,

$$g_i(x) = \int_{-\infty}^x f_i(t, a_i, d_i; n, \mathcal{P}_{\text{mag}}, \hat{L}_x^{\text{mag}}, F_{\text{lim}}) dt, \quad (9)$$

so that the new random variable is given by $\xi_i = g_i(x_i)$.

The distribution of ξ_i becomes uniform between 0 and 1 if the observation follows the assumed mode. Therefore, we have made statistical tests for uniformity of $\{\xi_i\}$. We apply the Kolmogorov-Smirnov (KS) test and the χ^2 -test. KS test for $\{\xi_i\}$ is straightforward by ksone (Press et al. 1992), while we provide N_{bin} -histogram with respect to ξ for χ^2 -test. After some trials, we find an appropriate bin size: we used two sets of 7-bins (equally spaced in ξ) for $a > 35.5$ and for $a < 35.5$, respectively. We have $N_{\text{bin}} = 14$ in total (detail is given

Appendix).

3.3. Treatment for the Upper Limit Data

In addition to the samples of the detected objects, we also analyze the samples including the upper limit data. If the upper limit is below the general trend, say $L_x \sim (10^{-2} - 10^{-3})L_{\text{rot}}$, they will improve the statistics. We use Sample SAB, i.e., Sample SAB_d and Sample SAB_{ul} are jointed.

We follow the general method to obtain a regression for the censored data as follows. Since we treat the data below the detection limit, we construct the probability density function that is obtained in the limit $F_{\text{lim}} \rightarrow 0$ by the simulator. We denote it by $\hat{f}_i(x)$, and its cumulative distribution by $\hat{g}_i(x)$. If x_i is the upper limit value, it is converted to $\hat{\xi}_i = \hat{g}_i(x_i)$, below which the actual value of ξ_i should take. Therefore, the observation ξ_i is set to be a randomly chosen value in between zero and $\hat{\xi}_i$. For all the objects in sample SAB_{ul}, we obtain a set of thus determined ξ_i . For detected values in Sample SAB_d, we simply have $\xi_i = \hat{g}_i(x_i)$. Note that this value is *not* $g_i(x_i)$ which is used previously for the detected values only. Thus, we have a set $\{\xi_i\}$ for the joint Sample SAB (Sample SAB_d + SAB_{ul}). The χ^2 test and the KS test are applied to $\{\xi_i\}$ of Sample SAB in the same way used for Sample SAB_d.

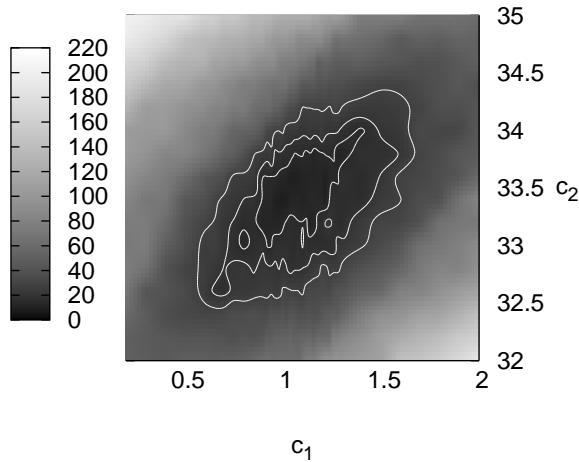


Figure 4. The χ^2 map for Sample SAB_d. The horizontal axis is the slope c_1 and the vertical axis is the normalization c_2 . The contours are drawn for the 1- σ (68.3%), 90%, and 99% confidence levels.

4. RESULTS

As the base line parameters of the simulator, we take $n = 3$, $\mathcal{P}_{\text{mag}} = 0$, $\sigma = 0.7$, and $\log F_{\text{lim}} = -14.0$. Actually this set is found to provide the best statistics after some trials. Using Sample SAB_d, we search for the most probable relation in the form of (3). The result is shown in the χ^2 map (Figure 4). The contours are drawn for 1- σ (68.3%), 90% and 99% confidence levels. We obtained the best fit model, $c_1 = 1.03$ and $c_2 = 33.36$, which is shown by the dashed line in Figure 1. Since the χ^2 map indicates a correlation between c_1 and c_2 with a slope of 1.62, we find

$$\log L_x = c_1(\log L_{\text{rot}} - 35.38) + 31.69, \quad (10)$$

with $c_1 = 1.03 \pm 0.27$. For the best fit model, we obtain $\chi^2/\text{dof} = 9.036/13$ and $D = 0.10419$ with $\mathcal{P}_{\text{KS}} = 56.60\%$.

Since we use non-parametric test, we also argue that the scatter around the regression line is reproduced well by our model. In a traditional way, the relation may be written as $L_x = 10^{-4.75} L_{\text{rot}}^{1.03}$, or more roughly, since $c_1 \approx 1$, the X-ray efficiency is constant; $\log \eta_{\text{psr}} = \log(L_x/L_{\text{rot}}) \approx -3.7$.

Let us consider dependence of the result on samples. We test the best fit model $(c_1, c_2) = (1.03, 33.36)$ on the two samples, Sample S_d and the joint sample S_d+A_d. We find that the best fit model fits very well to the both samples. For Sample S_d, we have $\chi^2/\text{dof} = 6.091/13$

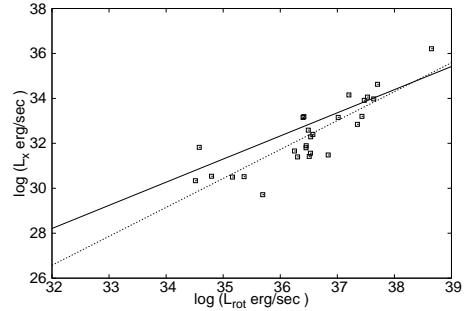


Figure 5. The $L_x - L_{\text{rot}}$ plot for Sample S_d. The solid line indicates the best fit relation, while the dotted line does the apparent regression line.

and $D = 0.09569$ with $\mathcal{P}_{\text{KS}} = 96.57\%$, and for Sample S_d+A_d, $\chi^2/\text{dof} = 5.424/13$, and $D = 0.099$ with $\mathcal{P}_{\text{KS}} = 74.7\%$. The best fit model is drawn by the solid line in Figure 5 for Sample S_d, and in Figure 6 for Sample S_d+A_d. In these figures, the regression lines obtained by the usual method are shown by the dotted lines. It is remarkable that the apparent regression lines dotted lines are different sample by sample, while the intrinsic relation is unchanged. This means that the apparent regression lines are influenced by selection effect, which is absorbed by the simulator, so that the both sample are best fitted by the single model.

There are two factors that affect the apparent regression line. Pulsars with large F_{rot} have high probability to be observed even if they have low luminosities. Such pulsars are present in $10^{35} \lesssim L_x \lesssim 10^{37}$ in Figure 5 distributing below the best fit $L_x - L_{\text{rot}}$ relation. This effect makes the regression line steeper as seen in Sample S_d. The same would occur if still deeper observations were made in future. On the other hand, if pulsars with small F_{rot} are included, say by adding Sample B or C, then the instrumental flux limit becomes important; namely dim pulsars such as observed in Sample S are difficult to be observed. Therefore, by adding data for pulsars with small F_{rot} (small L_{rot} and large distances), pulsars with large L_x are selectively included in the sample. This makes the apparent regression line flatter. This can be seen in Figure 6 (Sample S_d+A_d), i.e., more data appear above the regression line in the low L_{rot} regime ($10^{33} \lesssim L_{\text{rot}} \lesssim 10^{35}$). Therefore, the slope of the apparent regression line becomes flatter in Sample S_d+A_d. It is therefore notable that the slope of a apparent regression line is affected by properties of samples, and the simulation of the probability density $f_i(x)$ including individuality must be stressed.

Next we examine the dependence of the simulation parameters. The best fit model relation (10) is fixed,

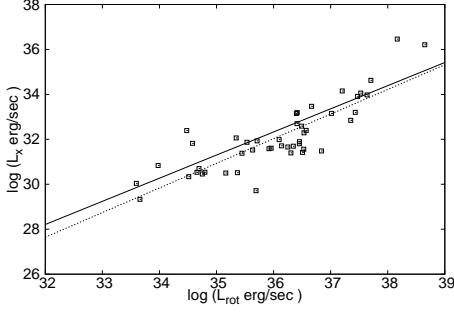


Figure 6. The same as Figure 5 but for the joint sample of S_d and A_d .

and the simulation parameters, n , \mathcal{P}_{mag} , σ , and F_{lim} , are changed separately to see how the test statistics changes. The result is summarized in Table 3.

Regarding the anisotropy parameter n , we find that on average the X-ray radiation comes neither from the whole neutron star nor from the hot region on the surface, and that anisotropy with $n \sim 2 - 3$ is preferred. The model of hot spot ($n = 1$) does not have a good fit to the data, though the test statics is marginal ($\mathcal{P}_{\text{KS}} = 14.48\%$). The result suggests that the X-ray radiation is beamed, rather than from a hot spot, for at least for some important fraction of the pulsars.

The scatter due to the uncertainty in distance and interstellar absorption is consistent with the estimate $\sigma = 0.7$, which is suggested by He et al.(2013) (see § 3.1). The acceptable value would be at most $\sigma \sim 0.9$ (see Table 3).

The detection limit is very much sensitive to the fitting. The acceptable value is very narrow. If $\log F_{\text{lim}} \gtrsim -13.5$, no acceptable model is found. We argue that regarding the detection limit of the instruments is very much important in a statistical study of L_x .

We examine whether the high-magnetic field pulsars, Sample HB, follows the best fit model. The result is summarized in Table 4. If we assume $\mathcal{P}_{\text{mag}} = 0$, the best fit parameters obtained for Sample SAB gives the statistics as $\mathcal{P}_{\text{KS}} = 0.09\%$ for Sample HB_d and $\mathcal{P}_{\text{KS}} = 4.65\%$ for the joint sample HB + SAB. Therefore, non existence of the excess emission is rejected for the both samples. In spite of the fact that sample HB is a subset of the rotation powered radio pulsars, they do not obey the best fit model for Sample SAB_d . As far as Sample HB_d is concerned, the χ^2 map in Figure 7 indicates $c_1 \sim 0$, i.e., no correlation with respect to L_{rot} . It may be argued from Table 4 that $\mathcal{P}_{\text{mag}} \gtrsim 0.1$ for the high-magnetic field pulsars, and $\mathcal{P}_{\text{mag}} \sim 0.05$ for the joint sample. This is just a reflection of the fact that out of 9 pulsars in Sample HB_d , 3 pulsars have large efficiency $L_x/L_{\text{rot}} > 0.1$.

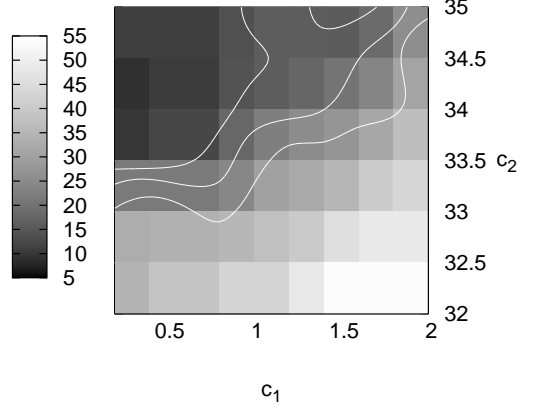


Figure 7. The same as Figure 4 but for Sample HB.

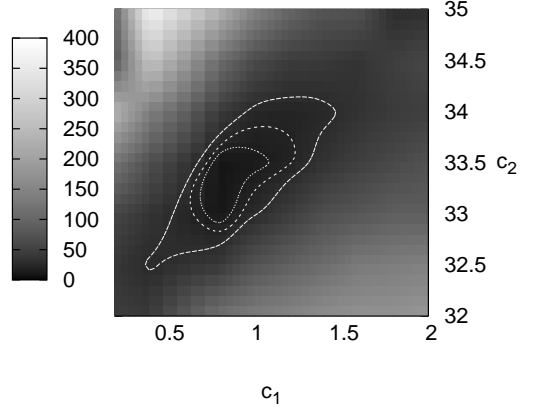


Figure 8. The same as Figure 4 but for the joint sample of S, A and B including the upper limit data.

If we add the upper limit data, Sample SAB_{ul} , to Sample SAB_d , the number of the pulsar is 99 in total (see Table 1). The χ^2 map for this joint sample is shown in Figure 8. The best fit model gives the test statistics, $\chi^2/\text{dof} = 14.091/13$ and $D = 0.09681$ with $\mathcal{P}_{\text{KS}} = 31.15\%$. From the χ^2 map, the most probable c_1 get slightly smaller and c_2 is slightly higher. The result of the sample including the upper limit yields $c_1 \approx 1.0$ and $c_2 \approx 33.5$, of which the test statistics is $\chi^2/\text{dof} = 12.75/13$ and $D = 0.05392$ with $\mathcal{P}_{\text{KS}} = 93.57\%$, in very good agreement with the result of Sample SAB_d .

Table 3. The result of χ^2 -test and KS test for different simulation parameters. The degree of freedom of χ^2 is 13.

n	χ^2	\mathcal{P}_{KS} (in %)	σ	χ^2	\mathcal{P}_{KS} (in %)	$\log F_{\text{lim}}$	χ^2	\mathcal{P}_{KS} (in %)
0	30.418	0.00	0.5	19.964	7.70	-13.0	97.600	0.00
1	10.236	14.48	0.6	16.600	25.97	-13.5	45.218	0.00
2	9.036	56.60	0.7	9.036	56.60	-14.0	9.036	56.60
3	12.545	42.19	0.9	10.164	19.30	-14.5	19.491	6.02
4	12.873	34.04	1.0	12.545	10.83	-15.0	24.109	0.30
6	15.673	31.46	1.3	16.291	2.48			

Table 4. χ^2 and KS significance level for the sample including the high-magnetic field pulsars.

Sample HB			Sample HB + SAB		
\mathcal{P}_{mag}	χ^2	\mathcal{P}_{KS} (in %)	\mathcal{P}_{mag}	χ^2	\mathcal{P}_{KS} (in %)
0.0	23.90	0.09	0.0	13.85	4.65
0.05	18.30	7.80	0.001	7.63	15.88
0.1	18.30	32.75	0.01	8.67	47.77
0.2	14.80	46.56	0.02	7.63	76.99
0.3	12.00	50.43	0.05	6.71	92.54
0.5	8.50	57.93	0.1	9.50	72.80
1.0	8.50	59.83	0.2	18.24	17.54
			0.4	24.54	0.21

5. DISCUSSION

To understand the distribution in the $L_x - L_{\text{rot}}$ plot, we take the following effects into account: (1) anisotropic radiation with randomly oriented viewing angles, (2) uncertainty in the distance estimate, and (3) detection limit mainly determined by the instruments. These effects obscure a possible intrinsic relation between L_x and L_{rot} . Regression lines which are obtained by the usual way are in general found to be different from the intrinsic $L_x - L_{\text{rot}}$ relation due to selection effect. Regarding the above effects with the Monte Carlo simulator, we have obtained the best fit model relation $L_x = 10^{-4.75} L_{\text{rot}}^{1.03}$. The scatter about the model relation is reproduced well by the Monte Carlo simulator; the χ^2 and KS test give very good statistics for the distribution.

There are three parameters, n , σ , and F_{lim} to reproduce the distribution. However, $\sigma \sim 0.7$ and $F_{\text{lim}} \sim 10^{-14} \text{ erg cm}^{-2} \text{ s}^{-1}$, so that only n can be We find the most probable value $n \sim 2$ (anisotropy with $F_x \propto \cos^2 \theta$.)

The above analysis is established for the samples in which the high-magnetic field pulsars ($B_d > 10^{13} \text{ G}$) are excluded. For Sample HB (high-magnetic field pulsar only), L_x seems not to correlate with L_{rot} at all. For

the joint sample, Sample HB+SAB, statistically acceptable models are obtained only if we introduce non-zero \mathcal{P}_{mag} ; namely there must be a finite probability of the excess X-ray radiation. The present Sample HB+SAB gives $\mathcal{P}_{\text{mag}} = 0.005$. The most likely source of the radiation would be magnetic field decay. In spite of the fact that the high-magnetic field pulsars emit radio pulses in the same way as the ordinary radio pulsars, they form a distinctive sub-class in the sense that they do not follow the model $L_x - L_{\text{rot}}$ relation that is established for the ordinary pulsars. Three high-magnetic field pulsars, which show the excess emission, J0726-2612, J1718-3718, and J1819-1458, possess very small values of F_{rot} , which are respectively $\log F_{\text{rot}} = -12.533$, -11.793 , and -12.240 . This means that Sample HB suffers strong selection effect. We cannot conclude the true probability \mathcal{P}_{mag} of magnetic heating at present. It will be obtained if we could have a complete sample within a given volume.

Let us next consider the reason why some pulsars in Sample SAB show high X-ray efficiency. To this end, we list the pulsars whose ξ is larger than 0.9: we have 10 pulsars in Table 5. Because the value of 10^{13} G used to define Sample HB is rather ad hoc, there may exist a pulsar showing an magnetic heating in the high- ξ pulsars. Another possibility is that there is unknown physics which makes ξ large. In addition to Table 5, we also provide a (ξ_i, a_i) plot for Sample SAB in Figure 9, which may be helpful to understand the distribution with respect to ξ .

Figure 9 shows that high- ξ pulsars distribute for all range of L_{rot} . The only exception is two very energetic pulsars, PSR B0540-69 and PSR B0531+21 (Crab), with $L_{\text{rot}} > 10^{38} \text{ erg s}^{-1}$ (indicated by "VE" in the Table 5). This may imply that the linearity of the $L_x - L_{\text{rot}}$ relation might not be hold for very energetic pulsars. But, the number of samples is too small to make the conclusion.

Of the remaining 8 pulsars, four pulsars have relatively large $\log F_{\text{rot}} \gtrsim -9$, while the remaining four have small $\log F_{\text{rot}} \lesssim -10$ (indicated by "H" and "L" in Table 5, respectively). In the large F_{rot} subset, PSR J1617-5055 and PSR J1400-6325 are observed in the hard X-ray

bands (> 20 keV) and classified as the soft gamma-ray pulsars (Kuiper & Hermsen, 2015). Photon indices are ~ 1 indicating their luminosity dominates in hard X and soft gamma-ray bands. However, neither are detected with *Fermi* LAT so that there must be a cut off in somewhere in MeV bands (Kuiper & Hermsen, 2015). The soft gamma-ray pulsars become high ξ pulsars because of their characteristic spectral energy distribution. On the other hand, PSR B0656+14 and PSR J1741-2054 are bright in thermal emission. These two with PSR B1055-52 are known as the neutron stars with high surface temperature in comparison with the standard cooling curve (Yakovlev et al. 2011, Karpova et al., 2014). For these pulsars, the spectrum can be fitted by one or two backbody with a less-luminous hard component fitted by the power law with indices typically of ~ 2 .

Among the four small F_{rot} pulsars, PSR B1055-52 is a bright source and studied well (De Luca et al. 2005, Posselt et al. 2015). Its X-ray spectrum is well fitted by two black body models plus a power law model. The dominant component is the black body with the temperature of 68 eV. PSR J0855-4644 shows a power law spectrum with photon index of 1.24, indicating this pulsar would belong to the soft gamma-ray type. For PSR B1822-14 and PSR J1301-6310, one needs better observational data to have finer spectral properties.

Although the number of sample is small, we can recognize two types of pulsars showing large X-ray efficiency. One is the soft gamma-ray type for which the rotational luminosity is dominated in the soft gamma-ray and hard X-ray bands. The other is the thermally bright type, which shows a high surface temperature as compared with the standard cooling curve. The luminosity is thought to originate from the neutron star with additional heating or suppressed cooling (Gusakov et al. 2004, Page et al. 2004). However, noticing that the high-magnetic field pulsars do not follow the $L_x - L_{\text{rot}}$ relation due to extra heating by the magnetic field and there are magnetars with small B_d , we suggest that the thermally bright type pulsars with high ξ are candidate objects that own dissipative magnetic field like magnetars. The objects plotted as magnetars in Figure 1 are in their active states. After the active phase or outbursts, majority of magnetars may reside in the distribution of the ordinary radio pulsars and may show high ξ .

It has been suggested (Kargaltsev et al. 2012) and quantitatively confirmed by our analysis that the probability density distribution $f(x)$ extends to smaller values of x ; namely, some pulsars appear very dim as compared with the model $L_x - L_{\text{rot}}$ relation. In our model, we simulate the distribution by the exponential form $f(x) = (1/n) \exp(x/n)$ as shown in the top left panel of Figure 3. The model is drawn as the geometrical effect.

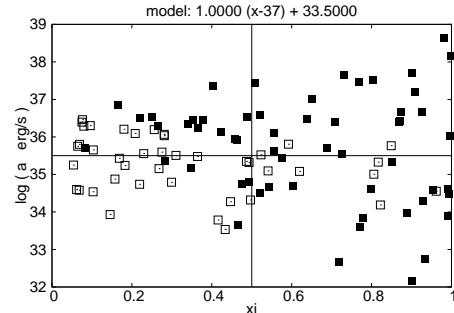


Figure 9. The scatter plot (ξ, a) for Sample SAB with the best fit model. The data of finite detection are indicated by the filled squares, while the upper limit data are indicated by the open square.

However, the reason of the extended distribution can be different. What we show is that if the distribution is assumed in this form, then the observed scatter is reproduced. As is pointed out by Kargaltsev & Pavlov(2008), similar things are found for the luminosity of PWN, i.e., some pulsar shows very small efficiency of the nebula emission. Vink et al. (2001) argue that the X-ray efficiency of PWN and that of the pulsar show similar behavior if they are plotted against the spin-down age. Taken from Table 2 of Kargaltsev & Pavlov(2008), the efficiencies of the pulsar and PWN, $\eta_{\text{psr}} = L_x/L_{\text{rot}}$ and $\eta_{\text{pwn}} = L_{\text{pwn}}/L_{\text{rot}}$, are plotted in Figure 10. Since the brightness of PWN is less dependent on the viewing angle, the wide distribution in η_{pwn} must not be caused by the viewing angle, but must be due to some unknown physics. It is noticeable that η_{psr} and η_{pwn} is positively correlated. This indicates that there is obviously at least one parameter other than L_{rot} , in other words, some unknown physics that governs the luminosity of both the pulsar and PWN. A possible link between the magnetospheric emission and the pulsar wind is pair multiplicity. If pairs are created efficiently, then the synchrotron emission from the magnetosphere in X-ray would be enhanced, and at the same time, the kinetic part of the energy carried by the wind would increase and causes a brighter PWN. This view is consistent with the fact that the $L_\gamma - L_{\text{rot}}$ correlation is tighter, i.e., the gamma-ray comes not from the secondary pairs but from the primary particles.

The high- ξ pulsars are also plotted in Figure 10. The soft-gamma type with high ξ follows the general trend (indicated by the crosses in Figure 10). The thermally bright pulsars show small η_{pwn} and large η_{psr} , i.e., they do not follow the general trend (indicated by the open circles in Figure 10). For these, although η_{psr} is large, the luminosity originates from the heat of the neutron star, and the efficiency of the magnetospheric emission is small so that the correlation holds even for these pulsars.

Further statistical analysis with much better quality of

Table 5. Large efficiency pulsars $\xi > 0.9$.

pulsar name	ξ	$\log L_{\text{rot}}$	$\log F_{\text{rot}}$	Fermi LAT	Hard X	Type	Spectral Properties		PWN η_{pwn}
							BB	PL	
B0540-69	0.998	38.17	-9.37	no	Yes	VE	-	PL(2.05)	-0.89
J0855-4644	0.994	36.02	-10.04	no	-	L,nth	-	PL(1.24)	-2.01
B1055-52	0.992	34.48	-9.97	Yes	-	L,th	2BB(68 eV)	-	-5.28
B0531+21	0.986	38.65	-6.03	Yes	Yes	VE	-	PL(1.63)	-1.64
B0656+14	0.969	34.58	-8.39	Yes	-	H,th	2BB(56 eV)	-	-5.68
J1301-6310	0.956	33.88	-10.82	no	-	L,?	?	?	-
B1822-14	0.931	34.61	-10.93	no	-	L,th?	BB(200 eV)	-	-
J1617-5055	0.922	37.20	-8.49	Yes	Yes	H,nth	-	PL(1.15)	-3.41
J1400-6325	0.918	37.70	-8.06	no	Yes	H,nth	-	PL(1.22)	-2.76
J1741-2054	0.901	33.98	-9.05	Yes	-	H,th	BB(60 eV)	-	-4.58

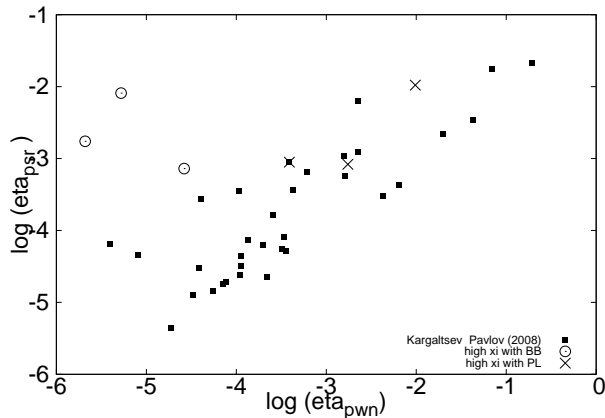


Figure 10. Correlation between the pulsar and pulsar wind nebula efficiency. The date of Kargaltsev & Pavlov(2008) are indicated by the filled squares. The high ξ pulsars of the thermally bright type (the open circles) and the soft gamma-ray type (the crosses) are also plotted.

data, separated into thermal, magnetospheric and PWN components, will give us finer discrimination of individual origins of emission, and a hint to find the unknown physics controlling the X-ray efficiencies.

We exclude MSPs from the samples. In the next step, we examine whether $L_x - L_{\text{rot}}$ plot of MSPs differs from that of the ordinary pulsars. The weak dipole field or small curvature radius of MSP may cause different dependence of pair creation rate on L_{rot} or other parameters. ‘Buried’ magnetic field by accreting matter may cause an additional heating. We may have a hit of these effect in the comparison.

The present work was supported in part by a Grant-in-Aid for Scientific Research (S.S. 25400221, AB 15K05107, TE 15H00845) from the MEXT. We thank H. Ohno for his helpful discussions and R. Shannon for carefully reading the draft and his comments.

APPENDIX

A. MODELING OF GEOMETRICAL EFFECTS

A simple model for the geometrical effect is obtained if we consider the case in which a small hot spot on the stellar surface is observed. Let the position vector of the spot, the observer’s direction and the angle between the two be respectively \mathbf{R} , \mathbf{i} , and θ . The observed flux may be given by $F_x = F_0 \cos \theta$, where F_0 is the observed flux when $\theta = 0$. Here we ignore the general relativistic effect. If we take F_x as an random variable, then the the probability distribution function $f(F_x)$ is defined such that the chance probability of observing the flux in between F_x and $F_x + dF_x$ is

$$\text{Pr.} = f(F_x)dF_x = f(F_x)F_0d(\cos \theta). \quad (\text{A1})$$

On the other hand, the probability for the spot to locate in between $\cos \theta$ and $\cos \theta + d(\cos \theta)$ is given by

$$\text{Pr.} = \frac{1}{4\pi} \left[d(\cos \theta) \int_0^{2\pi} d\phi \right] = \frac{d(\cos \theta)}{2}, \quad (\text{A2})$$

provided that the spot is randomly distributed on the surface. Comparing the two expression, we have, for $0 \leq F_x \leq F_0$,

$$f(F_x) = \frac{1}{2F_0} \quad (\text{A3})$$

else $f(F_x) = 0$, i.e., F_x distribute uniformly below F_0 . Note that $\int f(F_x)dF_x = 1/2$ because spots on the backside of the star would not be observed. The generalized expression is $F_x = F_0 \cos^n \theta$ with the anisotropy parameter n , where n larger than unity indicates the radiation is beamed. In the same way, we have, for $0 \leq F_x \leq F_0$,

$$f(F_x) = \frac{1}{2nF_0} \left(\frac{F_x}{F_0} \right)^{\frac{1}{n}-1}. \quad (\text{A4})$$

In general, the observer's direction has a finite angle to the emitting direction \mathbf{R} so that the observed flux tends to smaller than F_0 . In the Monte Carlo simulation F_0 is replaced by L_x^{model} , below which L_x is distributed according to the probability (A4). The distribution (A4) can be seen in the $L_x - L_{\text{rot}}$ plot as some dim pulsars are found below an expected correlation.

If the viewing angle to the rotation axis were given for each pulsar, a correction might be possible. However, we do not have convincing values of the viewing angles so that such a correction is difficult to made.

In the simulation, the random variable $x = \log F_x - \log F_0$ is used. The probability distribution function with respect to x and its cumulative distribution become, respectively,

$$f(x) = \frac{\ln 10}{n} 10^{x/n} \quad (\text{A5})$$

$$G(x) = \int_{-\infty}^x f(x') dx' = 10^{x/n}. \quad (\text{A6})$$

The random values which follow $f(x)$ are produced by random numbers G , which is distributed uniformly between one and unity, with

$$x = n \log G. \quad (\text{A7})$$

The viewing angle actually changes due to rotation according to

$$\cos \theta(t) = \cos \theta_0 \cos \zeta - \sin \theta_0 \sin \zeta \sin \Omega t, \quad (\text{A8})$$

where Ω is the angular velocity of the star, $\cos \zeta = \mathbf{i} \cdot \Omega$ indicates the observers direction and $\Omega = |\Omega|$. Since we treat the phase averaged flux, the mean value of $\cos^n \theta(t)$ should be used to evaluate the effective value of θ in the Monte Carlo simulator. However, we simply assume the randomly distributed observer and use the distribution (A4).

B. SPECTRAL ANALYSIS OF PSR J1909+0749

PSR J1909+0749 was observed serendipitously by *Chandra* on 2008 (ObsID 9614), February 28 using Advanced CCD Imaging Spectrometer (ACIS). The data reduction was done with the *Chandra* Interactive Analysis Observations (CIAO) software (version 4.7). The radio pulsar was imaged on the ACIS-S2 chip, 13' off-axis. No source was found on the chip by the CIAO `wavdetect` script. Therefore, we derived an upper limit on the count rate. To generate a new level-2 event file for the observation data, we made use of `Chandra_repro` preprocessing script. Next, we performed time filtering using `dmgti` and `deflare` scripts, and then the exposure-corrected image was created by `fluximage` scripts. We calculated the count rate by exposure-corrected image with `srcflux` scripts. The count rate was converted into the unabsorbed flux by using PIMMS, for which N_H value is obtained by $N_H(10^{20} \text{cm}^{-2}) = 0.30_{-0.09}^{+0.13} \text{DM}(\text{pc cm}^{-3})$ (He et al. 2013) and we used a power law model with a photon index of 1.5.

C. IMPROVEMENT OF χ^2 -TEST

We need to test the uniformity of $\xi_i \in [0, 1)$. Although this seems straightforward, it is found that χ^2 is not sensitive to the slope of the regression line, c_1 . The upper left panel of Figure C1 shows the scatter plots of (ξ_i, a_i) for the joint Sample SAB, where the model parameters are $c_1 = 1.0$, $c_2 = 33.4$, $n = 2$, $\mathcal{P}_{\text{mag}} = 0$, and $\log F_{\text{lim}} = -14.0$. One can see that the distribution with respect to ξ is more or less uniform. We find $\chi^2/\text{dof} = 8.4/9$. The middle and bottom plots represent the same plots but for different slopes, i.e., $(c_1, c_2) = (0.6, 33.0)$, and $(1.6, 33.8)$, respectively. Although the slopes are significantly different in the two cases, the distributions with respect to ξ again seem more or less uniform as far as one forgets about distributions with a . We have good values, $\chi^2/\text{dof} = 11.2/9$ and $9.8/9$, respectively. An important difference is asymmetry in quadrants of the diagram. In the middle plot (shallow slope), a larger population is seen in the quadrant with large ξ and large a and in the quadrant with small ξ and small a , while in the bottom plot (steep slope), a larger population is seen in the opposite quadrants. This tendency is also seen in the histograms (the right column of Figure C1) made separately for the two subsets with $a < a_c$ and with $a > a_c$, where we take $a_c = 35.5$.

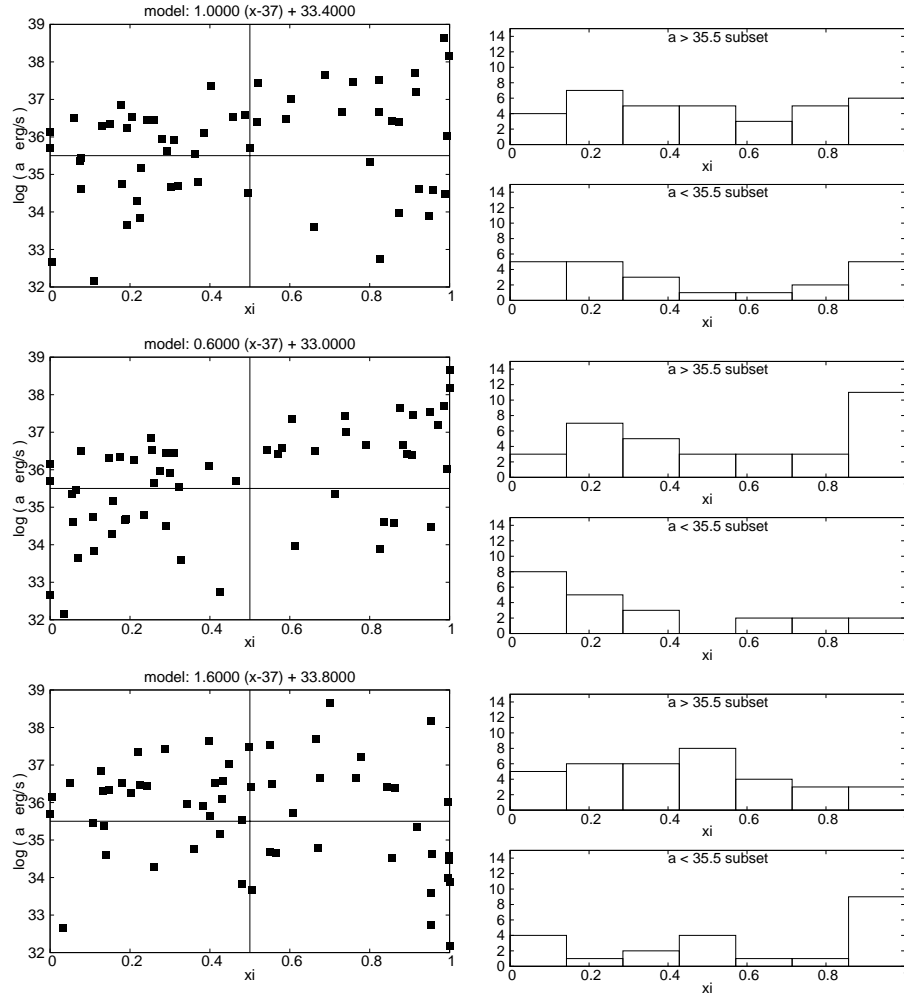


Figure C1. The plot of (ξ_i, a_i) for the sampled pulsars (left panels) and the histogram with respect to ξ (right panels) for three different model relations, from the top $(c_1, c_2) = (1.0, 33.4)$, $(0.6, 33.0)$, and $(1.6, 33.8)$.

A simple χ^2 test for uniformity of ξ is thus found insensitive to the slope. This degeneracy can be resolved if we see the distribution in the (ξ, a) plane. To have an sensitivity with respect to c_1 , we separate the data into two subset, i.e., a large- a subset and a small- a subset by $a_c = 35.5$. We prepare N_ξ bins for each subsets, and the χ^2 test is done for $2N_\xi$ -bins. A suitable number of the bin for the present sample is found to be $N_\xi = 7$.

REFERENCES

- Younes, G., Kouveliotou, C., & Roberts, O. 2016, GCN, 19736
 Kennea, J. A., Lien, A. Y., Marshall, F. E., et al. 2016, GCN, 19735
 Kiziltan, B., Kottas, A., De Yoreo, M., & Thorsett, S. E. 2013, ApJ, 778, 66
 Archibald, R. F., Kaspi, V. M., Tendulkar, S. P., & Scholz, P. 2016, arXiv:1608.01007
 Abdo, A. A., Ackermann, M., Ajello, M., et al. 2010, ApJ, 711, 64
 Abdo, A. A., Ajello, M., Allafort, A., et al. 2013, ApJS, 208, 17
 Acero, F., Gallant, Y., Ballet, J., Renaud, M., & Terrier, R. 2013, A&A, 551, A7
 Becker, W. 2009, Astrophysics and Space Science Library, 357, 91
 Becker, W., & Truemper, J. 1997, A&A, 326, 682
 Bejger, M., Fortin, M., Haensel, P., & Zdunik, J. L. 2011, A&A, 536, A87
 Bogdanov, S., Ng, C.-Y., & Kaspi, V. M. 2014, ApJL, 792, L36
 Camilo, F., Ray, P. S., Ransom, S. M., et al. 2009, ApJ, 705, 1
 Ciolfi, R., & Rezzolla, L. 2013, MNRAS, 435, L43
 De Luca, A., Caraveo, P. A., Mereghetti, S., Negroni, M., & Bignami, G. F. 2005, ApJ, 623, 1051
 Duncan, R. C., & Thompson, C. 1992, ApJL, 392, L9
 Esposito, P., Israel, G. L., Turolla, R., et al. 2010, MNRAS, 405, 1787
 Gavriil, F. P., Gonzalez, M. E., Gotthelf, E. V., et al. 2008, Science, 319, 1802
 Gotthelf, E. V., Halpern, J. P., & Alford, J. 2013, ApJ, 765, 58
 Gusakov, M. E., Kaminker, A. D., Yakovlev, D. G., & Gnedin, O. Y. 2004, A&A, 423, 1063
 Halpern, J. P., & Gotthelf, E. V. 2010, ApJ, 709, 436
 He, C., Ng, C.-Y., & Kaspi, V. M. 2013, ApJ, 768, 64

- Kaaret, P., Marshall, H. L., Aldcroft, T. L., et al. 2001, *ApJ*, 546, 1159
- Kargaltsev, O., & Pavlov, G. G. 2008, 40 Years of Pulsars: Millisecond Pulsars, Magnetars and More, 983, 171
- Kargaltsev, O., Durant, M., Pavlov, G. G., & Garmire, G. 2012, *ApJS*, 201, 37
- Karpova, A., Danilenko, A., Shibanov, Y., Shternin, P., & Zyuzin, D. 2014, *ApJ*, 789, 97
- Kennea, J., Cordova, F., Chatterjee, S., et al. 2002, arXiv:astro-ph/0202055
- Kuiper, L., & Hermsen, W. 2015, *MNRAS*, 449, 3827
- Li, X.-H., Lu, F.-J., & Li, Z. 2008, *ApJ*, 682, 1166
- Manchester, R. N., Hobbs, G. B., Teoh, A., & Hobbs, M. 2005, *AJ*, 129, 1993
- Marelli, M., De Luca, A., & Caraveo, P. A. 2011, *ApJ*, 733, 82
- Marthi, V. R., Chengalur, J. N., Gupta, Y., Dewangan, G. C., & Bhattacharya, D. 2011, *MNRAS*, 416, 2560
- McLaughlin, M. A., Rea, N., Gaensler, B. M., et al. 2007, *ApJ*, 670, 1307 1
- McGowan, K. E., Zane, S., Cropper, M., Vestrand, W. T., & Ho, C. 2006, *ApJ*, 639, 377
- Olausen, S. A., & Kaspi, V. M. 2014, *ApJS*, 212, 6
- Olausen, S. A., Zhu, W. W., Vogel, J. K., et al. 2013, *ApJ*, 764, 1
- Ozel, F., Psaltis, D., Arzoumanian, Z., Morsink, S., & Baubock, M. 2015, arXiv:1512.03067
- Page, D., Lattimer, J. M., Prakash, M., & Steiner, A. W. 2004, *ApJS*, 155, 623
- Pivovaro, M., Kaspi, V., & Gotthelf, E. 1998, *Science with XMM*, 83
- Porquet, D., Decourchelle, A., & Warwick, R. S. 2003, *A&A*, 401, 197
- Posselt, B., Spence, G., & Pavlov, G. G. 2015, *ApJ*, 811, 96
- Possenti, A., Cerutti, R., Colpi, M., & Mereghetti, S. 2002, *A&A*, 387, 993
- Press, W.H., Flannery, B.P., Teukolsky, S.A., & Vetterling, 1992, *Numerical Recipes in FORTRAN 77*, 2nd Edition (Cambridge, Cambridge University Press)
- Prinz, T., & Becker, W. 2015, arXiv:1511.07713
- Ray, P. S., Kerr, M., Parent, D., et al. 2011, *ApJS*, 194, 17
- Rea, N., Esposito, P., Turolla, R., et al. 2010, *Science*, 330, 944
- Rea, N., Israel, G. L., Pons, J. A., et al. 2013, *ApJ*, 770, 65
- Renaud, M., Marandon, V., Gotthelf, E. V., et al. 2010, *ApJ*, 716, 663
- Safi-Harb, S., & Kumar, H. S. 2008, *ApJ*, 684, 532-541
- Saito, Y. 1998, Ph.D Thesis, Univ. of Tokyo
- Seward, F. D., & Wang, Z.-R. 1988, *ApJ*, 332, 199
- Speagle, J. S., Kaplan, D. L., & van Kerkwijk, M. H. 2011, *ApJ*, 743, 183
- Takata, J., Wang, Y., & Cheng, K. S. 2011, *MNRAS*, 415, 1827
- Tepedelenhoğlu, E., Ögelman, H. 2005, *ApJL*, 630, L57
- Turolla, R., Zane, S., & Watts, A. L. 2015, *Reports on Progress in Physics*, 78, 116901
- Viganò, D., Rea, N., Pons, J. A., et al. 2013, *MNRAS*, 434, 123
- Vink, J., Bamba, A., & Yamazaki, R. 2011, *ApJ*, 727, 131
- Yakovlev, D. G., Ho, W. C. G., Shternin, P. S., Heinke, C. O., & Potekhin, A. Y. 2011, *MNRAS*, 411, 1977
- Zhu, W., Kaspi, V. M., Gonzalez, M. E., & Lyne, A. G. 2009, *ApJ*, 704, 1321
- Zhu, W. W., Kaspi, V. M., McLaughlin, M. A., et al. 2011, *ApJ*, 734, 44